Few layered black phosphorus/MoS$_2$ nanohybrid: A promising co-catalyst for solar driven hydrogen evolution

D. Amaranatha Reddy, Eun Hwa Kim, Madhusudana Gopannagari, Yujin Kim, D. Praveen Kumar, Tae Kyu Kim*

Department of Chemistry and Chemistry Institute of Functional Materials, Pusan National University, Busan 46241, Republic of Korea

ABSTRACT

Exploring active and stable photocatalysts is an essential requirement for boosting the efficiency of photocatalytic water splitting to obtain clean hydrogen fuel. Here, a few layered black phosphorus/MoS$_2$ (BP-MoS$_2$) nanohybrid was successfully prepared and verified it for photocatalytic hydrogen evolution using CdS nanorods as light absorbers. The resulting nanohybrids manifest remarkable catalytic performance with high amount of H$_2$ production (CdS/BP-MoS$_2$: 183.24 mmol h^{-1} g^{-1}) and outstanding catalytic stability. The observed amount of H$_2$ is much higher than that of various CdS/BP and CdS/MoS$_2$ based nanohybrids reported earlier. We expect that the demonstrated new heterostructured design strategy may bring novel insights to develop low-price noble metal free photocatalysts for hydrogen evolution.

1. Introduction

A clean hydrogen (H$_2$) fuel produced by splitting of water using free and plentiful solar energy is considered as an ideal solution to resolve the global renewable energy demand and environment problems [1]. Particularly, photocatalytic solar driven water splitting by applying semiconductor nanostructured materials has proved as a green, low-price and sustainable strategy for H$_2$ production [2]. Considering this over the past decades, numerous revolutionary semiconductor low dimensional photocatalysts have been formulated and affirmed it for H$_2$ evolution reactions [3–7]. But unfortunately, none of them are at a stage for commercial utilization due to their high price, low light harvesting capability, high recombination rate, low chemical stability and low quantum efficiency [8,9]. Thus it is an urgent need to develop low price noble metal free highly efficient solar driven semiconductor photocatalysts for H$_2$ production.

Recently black phosphorous (BP) a metal free semiconductor nanostructure have attracted a surge of interest in photocatalytic hydrogen evolution reactions because of their suitable band gap and promising electro and optical properties [10]. In particular the thickness dependent tuneable band gap nature from a value of 0.3 eV to 2 eV makes it suitable for light harvesting from visible to mid-infrared wavelength range and thus renders a great promise for sunlight driven photocatalytic water splitting [11,12]. For instance, Zhu et al. reported BP nanosheets as a visible light harvesting catalyst for H$_2$ production,

and found that the H$_2$ evolution rate (512 μmol h^{-1} g^{-1}) is ≈18 times larger than that of as-synthesized bulk BP nanostructures [13]. Zhao et al. synthesized BP nanosheets from the red phosphorous microsphere and noticed hydrogen evolution rate (6.9 μmol h^{-1}) is 203.2 times larger than that of red P nanoparticles (0.034 μmol h^{-1}) [14]. Noteworthy, the observed hydrogen evolution rates in previous reports are very low due to its low band gap and high rapid recombination rate, so the H$_2$ evolution performance of BP nanostructures needed to be further improved. To overcome these drawbacks, strategies such as doping with metal or non-metal ions, adding suitable co-catalysts nanostructures and forming nanohybrids with suitable nanostructures have been recently developed [15–20]. The results demonstrated that the formation of nanohybrids provides a large room to enhance the photocatalytic activity towards high efficiency and higher quantum yields by reducing the charge recombination rate [15–20].

Considering the importance of nanohybrids formation with BP recently several nanohybrids such as BP/g-C3N$_4$ [15], BP/WS$_2$ [16], Zn$_x$Cd$_{1-x}$S/phosphorene [17], BP/Pt-RGO [18], CdS/BP [19], BP/Au-La$_2$Ti$_2$O$_7$ [20] are developed and noticed improved H$_2$ evolution rate. We believe that compared to the above studied nanohybrids, the formation of atomically thin two-dimensional nanohybrids consist of metal free BP nanosheets and a highly active earth abundant MoS$_2$ nanostructures offer exciting possibilities to direct the electron flow on the heterojunctions and effectively separate photo charge carriers to hinder their recombination rate and promote H$_2$ evolution [21].

Moreover, the formation of nanohybrid brings numerous active sites, high mobility, high conductivity, and full spectrum light harvesting capability. Considering these peculiar interesting properties of BP-MoS$_2$ nanostructures, they have been extensively utilized for several applications such as field-effect transistors [22,23], electrochemical hydrogen evolution reactions [21] and optoelectronic devices [24,25]. However, their usage in photocatalytic H$_2$ production systems remains almost unexplored; this has incited us to take up the present study.

Herein, for the first time, a few layered BP-MoS$_2$ nanohybrids was designed using a simple ultrasonication combined with hydrothermal method and resultant nanohybrids are verified it for photocatalytic hydrogen evolution using CdS nanorods as light absorbers. Benefiting from the rich active sites, abundant structural and compositional features, the resulting nanohybrids manifest remarkable catalytic performance with high amount of H$_2$ production (CdS/BP-MoS$_2$: 183.24 mmol h^{-1} g^{-1}) and outstanding stability under sunlight irradiation. Such a significantly high hydrogen evolution rate is thoroughly explored by photocurrent and impedance analyses. We anticipate that more prominent sunlight-harvesting capability and highly reduced recombination rate are key factors for the enhancement of hydrogen production. Furthermore, the noticed amount of H$_2$ production rate is much larger than those of several black phosphorous and MoS$_2$ based CdS nanohybrids reported earlier. We expect that the demonstrated new heterostructured design pathway may bring novel insights to develop low-price photocatalysts for H$_2$ production.

2. Results and discussion

The fabrication procedure of few layered BP-MoS$_2$ and CdS/BP-MoS$_2$ nanohybrids is illustrated in Scheme 1. First, black phosphorus was synthesized using red phosphorous as the starting material using ultrasonication technique which is similar to previously reported method with a few modifications (Electronic Supplementary Information (ESI) for experimental details) [26]. Then, the as synthesized BP nanostructures were reacting with an appropriate amount of Na$_2$MoO$_4$ and C$_2$H$_5$NS by hydrothermal method to obtain BP-MoS$_2$ nanohybrid. Finally, the bulk BP-MoS$_2$ nanohybrid was transformed to few layered BP-MoS$_2$ nanostructures through an ultrasonication technique. Alternatively, 1D CdS nanorods are synthesized through hydrothermal method by reacting Cd and S sources using ethylenediamine as a solvent. Finally, BP-MoS$_2$/CdS nanohybrids were prepared by a chemical solution treatment with the aid of strong ultrasonication.

Field-emission transmission electron microscopy (FETEM) micrographs present the well-defined nanosheets like morphology of the as-synthesized BP with thickness of about 80 nm (Fig. S1(a)). A representative HRTEM image evidently shows lattice diffraction patterns with an inter-planar length of 0.21 nm, representing to the (002) plane of BP (Fig. S1(b)). Figs. S1(c) and S1(d) show the TEM images of MoS$_2$,

having layered structure with interlayer spacing of 0.62 nm with 9 layers of thick (Fig. S1(d)). The BP-MoS$_2$ nanohybrid shows both the lattice diffraction patterns of the BP (0.21 nm) and MoS$_2$ (0.619 nm) nanosheets (Figs. S1(e) and S1(f)). Elemental mappings of BP-MoS$_2$ nanohybrid show P, Mo and S elements are uniformly distributed throughout the sample (Fig. S2(a)–(f)), which demonstrates the successful formation of hybrid nanostructures of BP-MoS$_2$. To confirm whether the nanohybrid is composed of both BP and MoS$_2$ with layered structure, we performed energy dispersive spectroscopy (EDS) mapping for individual BP-MoS$_2$ layers. Fig. S3(a)–(f) indicate that few layered nanohybrid are composed of both BP and MoS$_2$. Finally, the thickness of the synthesized BP-MoS$_2$ nanohybrid was measured using atomic force microscopy (AFM) analysis (Fig. S4), which indicates that the nanohybrid is comprise a few layers with an approximate thickness of 8 nm.

Next, the formed CdS and CdS/BP-MoS$_2$ morphology and structured was verified by field emission scanning electron microscopy (FESEM) and FETEM. As shown in Fig. S5, the as-synthesized CdS nanostructures show rod like morphology with an average length of 200 nm. After the chemical reaction with BP-MoS$_2$, the CdS nanorods are covered with few layered BP-MoS$_2$ nanostructures (Fig. 1(a)–(c)). Most of the BP-MoS$_2$ nano-layers are attached on the edges of CdS nanorods, which possibly indicative of strong attractive forces between exposed (0 0 1) side of the CdS nanorods and sulfur layers in the BP-MoS$_2$ nanohybrid. The anchoring capacity was much higher in the edge sides compared to the surface of the CdS nanorods. In addition, elemental mappings micrographs of single CdS/BP-MoS$_2$ nanorods demonstrate the homogenous length wise dispersion of Cd, S, P, and Mo elements in the nanohybrid (Fig. 1(d)–(i)).

The X-ray photo electron spectroscopy (XPS) was conducted to clarify the nanohybrid formation and purity of the synthesized nanostructures. The XPS survey spectrum in Fig. S6(a) clearly indicates that the BP-MoS$_2$ nanohybrid is consisted of P, Mo and S elements. P 2p XPS spectrum (Fig. S6(b)) can be deconvoluted into three peaks; P 2p$_{3/2}$ (129.40 eV), P 2p$_{1/2}$ (130.24 eV), and a small peak at around 134.05 eV (can be assigned to oxidized phosphorus (P$_x$O$_y$)) [27]. As shown in Fig. S6(c), the bands located at the core level binding energy of 229.51 and 232.71 eV, can be assigned to the doublet Mo^{4+} 3d$_{5/2}$ and 3d$_{3/2}$ states, respectively [28]. Similarly, the peaks located at binding energies of 162.28 (S 2p$_{3/2}$) and 163.46 eV (S 2p$_{1/2}$) suggest the S^{2-} species in the BP-MoS$_2$ nanohybrid (Fig. S6(d)) [29]. As shown in Fig. 2(a)–(e), in addition to P, S and Mo elements, Cd 3d peaks (403.02 and 411.18 eV, assigned to the Cd 3d$_{5/2}$ and Cd3d$_{3/2}$, respectively) are observed in the CdS/BP-MoS$_2$ nanohybrid [29]. All these findings strongly evidence that the as-prepared nanohybrid contains BP-MoS$_2$ and CdS without any other impurities. The structural and phase purity of as-prepared CdS, CdS/MoS$_2$, CdS/BP and CdS/BP-MoS$_2$ nanohybrids were measured using X-ray diffraction (XRD) (Fig. 2(f)). The diffraction peaks demonstrate that CdS nanostructures show perfect hexagonal structure. In
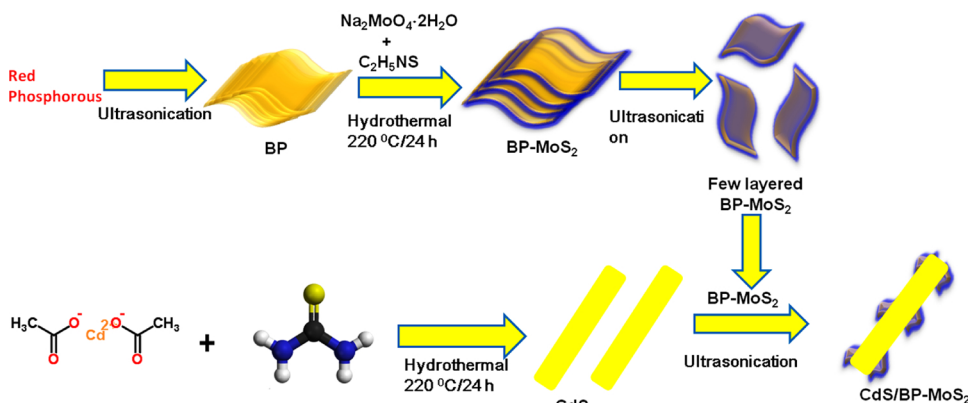
Scheme 1. Schematic illustration of the formation of few layered CdS/BP-MoS$_2$ nanohybrid. Step I: Formation of the BP nanostructures using red phosphorous through ultrasonication technique. Step II: Formation of BP-MoS$_2$ nanohybrid using hydrothermal method at 220 °C/24 h. Step III: Ultrasonication of the BP-MoS$_2$ nanohybrid to produce few layered nanosheets. Step IV: Synthesis of CdS nanorods. Step V: Formation of CdS/BP-MoS$_2$ nanohybrid by ultrasonication combined with homogenous chemical process.
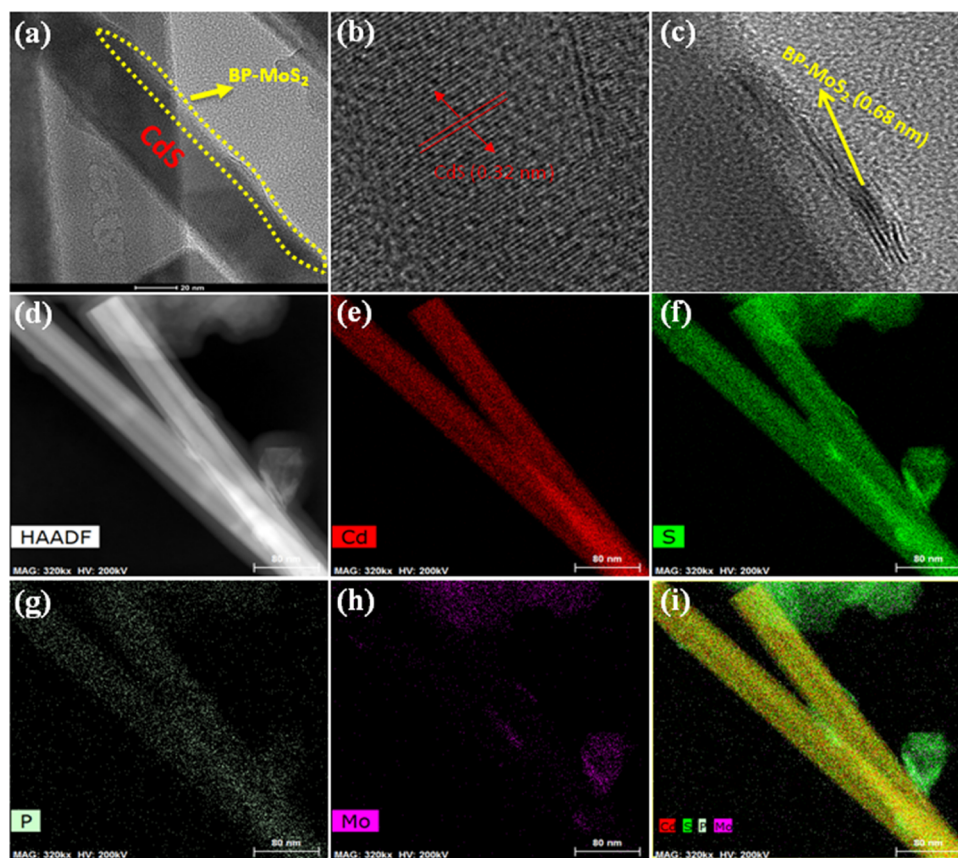
Fig. 1. (a) FETEM image of CdS/BP-MoS$_2$ nanohybrid. ((b) and (c)) HRTEM image of corresponding Cd and BP-MoS$_2$ nanostructures, respectively. ((d)–(i)) HAADF image (d) and elemental mapping micrographs of CdS/BP-MoS$_2$ nanohybrid, showing the presence of (e) Cd, (f) S, (g) P, (h) Mo, and (i) all elements.

addition, after immobilized with co-catalysts (BP, MoS$_2$, and BP-MoS$_2$), the CdS nanostructures does not alter the crystal phase of the CdS nanorods [28].

The solar driven photocatalytic hydrogen evolution rate of all the synthesized nanostructures were examined under simulated sunlight irradiation (AM 1.5 G) using sacrificial hole scavenger (lactic acid). Initial photocatalytic experiments were carried out using BP, MoS$_2$ and BP-MoS$_2$ nanostructures. We noticed that a very little amount of hydrogen was evolved with MoS$_2$ (0.05 mmol h^{-1} g^{-1}), BP (0.2 mmol h^{-1} g^{-1}) and BP-MoS$_2$ (0.716 mmol h^{-1} g^{-1}) nanostructures (Fig. S7); it may be ascribed to the limited light harvesting capacities [30,31]. However, we noticed that BP-MoS$_2$ nanostructures exhibit higher hydrogen evolution rate than those of MoS$_2$ and BP.

To maximize the photocatalytic rate of above BP-MoS$_2$ nanostructures, the different wt.% of BP modified MoS$_2$ nanocomposites were synthesized and interacted on CdS nanorods. The relevant nanohybrids were assessed under the similar experimental conditions and obtained results are presented in Fig. S8. 10 wt.% BP modified MoS$_2$ nanostructures integrated on CdS showing highest value (183.24 mmol h^{-1} g^{-1}) compared to other nanostructures. We have used 10 wt.% BP-MoS$_2$ nanostructures as a co-catalyst for further photocatalytic assessments.

To understand the role of integrated amount of BP-MoS$_2$ on CdS nanorods, the solar driven photocatalytic activity of CdS nanostructures with different wt.% of BP-MoS$_2$ (0–12 wt.%) was examined under the very similar conditions and the photo-catalytically produced amount of H$_2$ is shown in Fig. 3(a). As-synthesized CdS nanostructures shows a very low solar driven photocatalytic H$_2$ evolution rate (2.54 mmol h^{-1} g^{-1}), which may be due to low band gap and high recombination rate. In contrast, the formation of nanohybrid with BP-MoS$_2$ obviously improves the solar driven photocatalytic activity. The optimal CdS/BP-

MoS$_2$ (8 wt.%) nanohybrid shows a super high H$_2$-production of 183.24 mmol h^{-1} g^{-1}, which is 72.14 times larger than that of CdS nanostructures. The identical experiments repeated up to five times, showing almost the same photocatalytic performance (Fig. 3(c)). The observed amount of evolved H$_2$ is much higher than the CdS/BP and CdS/MoS$_2$ nanostructures (Fig. 3(b)). Furthermore, the observed amount of hydrogen production is much even higher than noble metal Pt integrated CdS nanorods (34.98 mmol g^{-1} h^{-1}), entailing that the developed MoS$_2$-BP co-catalyst nanostructures is for better than that of high price noble metal Pt nanostructures (Fig. S9).

Moreover, the H$_2$ evolution rate is much higher in comparison with earlier reported BP, MoS$_2$ and their related nanohybrids (Table S1). However, for the cases of high BP-MoS$_2$ loading amounts (> 8 wt.%) on the CdS nanostructures surface, the photocatalytic H$_2$ production rates are decreased (Fig. 3(a)). In these cases, BP-MoS$_2$ nanosheets may suppress the photogenerated electrons, resulting decreased the H$_2$ evolution rate [32]. Moreover, the lower loading amount of BP-MoS$_2$ also exhibit a diminished H$_2$ evolution rate, which can be ascribed to the fewer active sites in the nanohybrid.

To understand the importance of light source, role of different hole scavengers, hole scavenger amount and photocatalyst (CdS/BP-MoS$_2$) dosage on the photocatalytic hydrogen evolution rate, the photocatalytic assessments under different experimental conditions have been performed (Figs. S10 and S11). Fig. S10 shows the hydrogen evolution rate of CdS/BP-MoS$_2$ under different light wavelengths, namely UV (< 425 nm), visible (> 425 nm), NIR (> 700 nm) and solar light (AM 1.5 G). Nanostructures under UV and NIR light irradiations exhibit a very lower hydrogen evolution rates than that under VIS light condition. The DRS results also evidenced that the synthesized nanostructures have capable of high visible light harvesting capacity than the other light wavelengths. Interestingly, the hydrogen evolution rate is
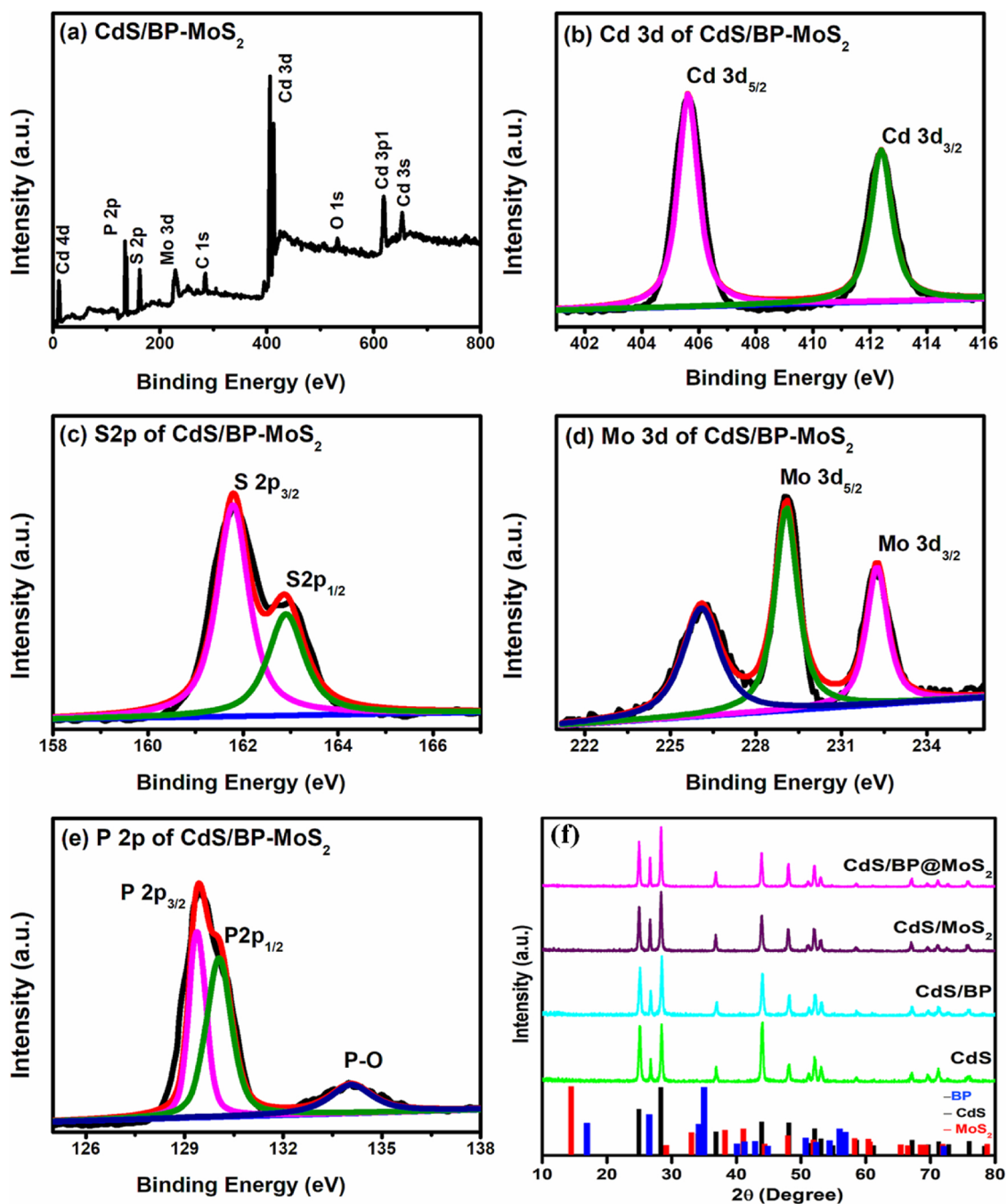
Fig. 2. (a) XPS survey spectrum and core-level XPS spectra of (b) Cd 3d, (c) S 2p, (d) Mo 3d, and (e) P 2p of CdS/BP-MoS$_2$ nanohybrid. (f) Measured XRD patterns of CdS, CdS/BP, CdS/MoS$_2$ and CdS/BP-MoS$_2$ nanocomposites with standard cards of BP, CdS and MoS$_2$.

highest under solar light, which indicates that the synthesized nanostructures having the light harvesting capacity from UV–vis-NIR. However, the UV and NIR light contribution are less than the visible light.

Fig. S11(a) shows the influence of catalyst dosage (from 1 mg to 30 mg) on a solar driven hydrogen production for CdS/BP-MoS$_2$ in an aqueous lactic acid (20% volume) solution. 1 mg of the optimized photocatalyst dosage displays the best catalytic performance. When the catalyst dosage increases, the hydrogen evolution rate gradually decreases, possibly due to blocked or scattered light by the excess suspended photocatalysts in the reaction medium [33]. Fig. S11(b) shows the photocatalytic H$_2$ production rates as a function of different amount of hole scavenger (lactic acid) concentrations. It indicates that the hydrogen evolution rate gradually increases when the lactic acid

concentration raises up to 3 mL. The reduction in the hydrogen evolution rate in high lactic acid concentration (> 3 mL) may be due to high viscosity and a large number of molecules in the reaction medium, reducing the light harvesting capacity of the nanocomposites [34]. In addition, in order to understand the selection of scavengers for an efficient hydrogen evolution rate, different hole scavengers such as methanol, ethanol, triethanolamine (TEOA) and Na$_2$S-Na$_2$SO$_3$ were verified and supported the fact that lactic acid is the one of the best scavengers for efficient hydrogen evolution in the present system (Fig. S11(c)). The optimized nanostructures were verified under aerobic condition for the practical application point of view (Fig. S11(d)) and provided the relatively low amount of hydrogen productions (126.52 mmol h^{-1} g^{-1}) amount of hydrogen. The noticed lower amount (than the inert condition) may indicate that backward reactions occur
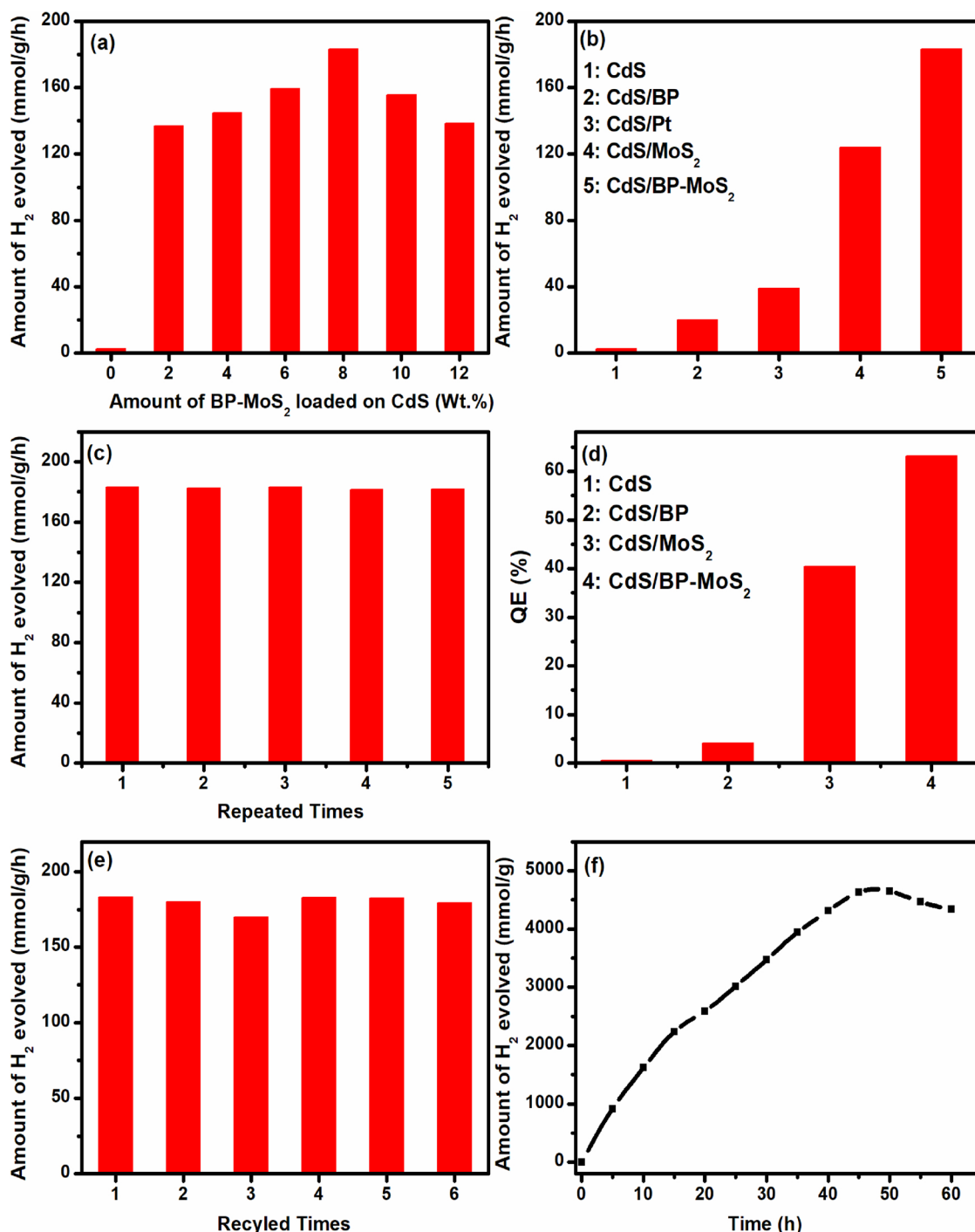
Fig. 3. Amount of H_2 evolved in 15 ml of aqueous solution containing lactic acid (3 mL) and DI water (12 mL), with suspended CdS/BP-MoS$_2$ containing 0, 2, 4, 6, 8, and 10 wt% BP-MoS$_2$ loaded on CdS nanostructures. (b) Comparison of CdS/BP-MoS$_2$ H_2 evolution rate with CdS, CdS/BP, CdS/Pt, and CdS/MoS$_2$ nanocomposites. (c) Amount of H_2 evolved with CdS/BP-MoS$_2$ nanocomposites under identical experimental conditions, repeated five times. (d) Comparison of the QE of CdS/BP-MoS$_2$ with CdS, CdS/BP, CdS/MoS$_2$, CdS/BP-MoS$_2$. (e) Hydrogen production in recycling experiments using the optimized CdS/BP-MoS$_2$ nanohybrid. (f) Long-term stability of the optimized CdS/BP-MoS$_2$ nanohybrid.

under aerobic conditions, resulting decreased the H_2 production rate.

In addition to photocatalytic H_2 production rate, the apparent quantum yield (AQEs) is another crucial parameter for assessing photocatalytic performance. We have measured AQEs of optimized CdS/BP-MoS$_2$ nanostructures under different wavelengths of light sources from UV to NIR (Fig. S12). It is clear that the synthesized nanostructures exhibit highest AQEs in between 425 nm to 500 nm, while the AQEs in UV or NIR are very low. DRS results also evidenced that the synthesized nanostructures have capable of high visible light harvesting

capacity than the other light wavelengths. In addition, CdS, CdS/BP, CdS/MoS$_2$, CdS/BP-MoS$_2$ nanohybrids were evaluated by visible-light irradiation using a 425 nm band pass filter, and the estimated QEs were around 0.535, 4.13, 40.5 and 63.1%, respectively (Fig. 3(d)).

Photocatalytic recycling analysis was carried out to assess the catalytic stability of the optimized CdS/BP-MoS$_2$ nanohybrid up to six recycles (Fig. 3(e)). Almost similar amounts of H_2 were evolved in all the recycling measurements; while a small decrease was observed in the third recycling process due to the decreased scavenger concentration

upon its conversion to pyuic acid during the photocatalytic reaction. However, after adding extra 3 ml of lactic acid, the amount of H_2 evolution is similar to the first cycle. Moreover, to check the stability of photocatalysts, the long-term assessments over 55 h were conducted (Fig. 3(f)). The results demonstrate that the photocatalytic hydrogen evolution rate was increased steadily with respect of time up to 45 h and then decreased. The slight decres in H_2 evolution rate may be due to filing of huge amount of hydrogen and deficiency in hole scavenger due to oxidation of lactic acid to pyruic acid during long reaction time. To further assess the stability of photocatalysts, we evacuated the gas produced in the photo-reactor and added the fresh 3 ml of lactic acid. Then, we performed photocatalytic assessments over successive 30 h (Fig. S13). The results demonstrated that the evolution rate of H_2 remained similar to that in the first 20 h and then decreased, indicating that the synthesized nanohybrid is highly stable. Moreover, XRD results (Fig. S14) clearly demonstrated that the crystal structure of the CdS/BP-MoS_2 nanohybrid remained unchanged after recycling measurement; this indicates that the nanohybrid is stable for photocatalytic H_2 production.

To unravel the origin of the remarkable hydrogen evolution rate and photo-stability of the CdS/BP-MoS_2 nanohybrid, the light harvesting capacity, photo charge carriers separation and migration, and surface redox reactions were exhaustively characterized by UV–vis-NIR spectroscopy, photoluminescence (PL), photo-induced current measurements, electrochemical impedance spectroscopy (EIS) and BET analysis. Firstly, the light harvesting capability of BP, MoS_2, and BP-MoS_2 nanostructures were measured by UV–vis-NIR spectroscopy (Fig. S15). As showed in Fig. S15(a), the BP nanostructure shows a very wide absorption ranging from UV to NIR region, where a smaller absorption maximum was noticed at around 970 and 320 nm [13]. Moreover, the stronger UV absorption (than NIR) indicates the formation of thin few layered BP nanosheets, which requires more energy for the electron transition [35]. The UV-VIS-NIR absorption spectrum of MoS_2 nanosheets (Fig. S15(b)), exhibit excitonic absorption bands located at around 688 and 629 nm, which are associated to the spin orbit splitting of the top of the valence band (VB) at the K point of the Brillouin zone in MoS_2 and arise from the bonding interaction of laterally extended Mo 4d orbitals with S 3p orbitals. Furthermore, two more absorption peaks are noticed at around 492 and 296 nm related to a direct transition from energy levels deep in the VB to the conduction band (CB) [36,37]. The BP-MoS_2 nanohybrids shows both MoS_2 and BP absorption bands (Fig. S15(c)), indicating the formation of hybrid nanostructures. Based on the above results, it is clear that BP-MoS_2 nanostructures have the light harvesting capability from UV to NIR ranges. To assess the above speculation, the photocatalytic hydrogen evolution measurement was carried out under UV, VIS and NIR light irradiation with optimized experimental conditions (photocatalyst BP-MoS_2: 1 mg, lactic acid: 3 mL) and the obtained results are presented in Fig. S16. BP-MoS_2 nanostructures utilize light energy in all wavelengths ranging from UV to NIR and contribute those energies for the photocatalytic H_2 production. Energy band gaps of BP, MoS_2 and BP-MoS_2 nanostructures were measured from their Tauc plots (Fig. S17), and was estimated to be 2.10, 1.69 and 1.97 eV, respectively. The as-prepared CdS, CdS/BP, CdS/MoS_2 and CdS/BP-MoS_2 nanohybrids show sharp absorption edges at around 502–509 nm (Fig. 4(a)). The small shift in the absorption maxima may be due to interaction between CdS and co-catalyst materials. Moreover, the integrating co-catalyst on CdS nanorods shows much enhanced absorption intensity, demonstrating higher capability of light harvesting nature in the composites than bare CdS. The estimated band gap values are 2.46, 2.45, 2.44, 2.438 eV for CdS, CdS/BP, CdS/MoS_2 and CdS/BP@MoS_2 nanocomposites, respectively.

To acquire information on possibilities of photo-induced charge
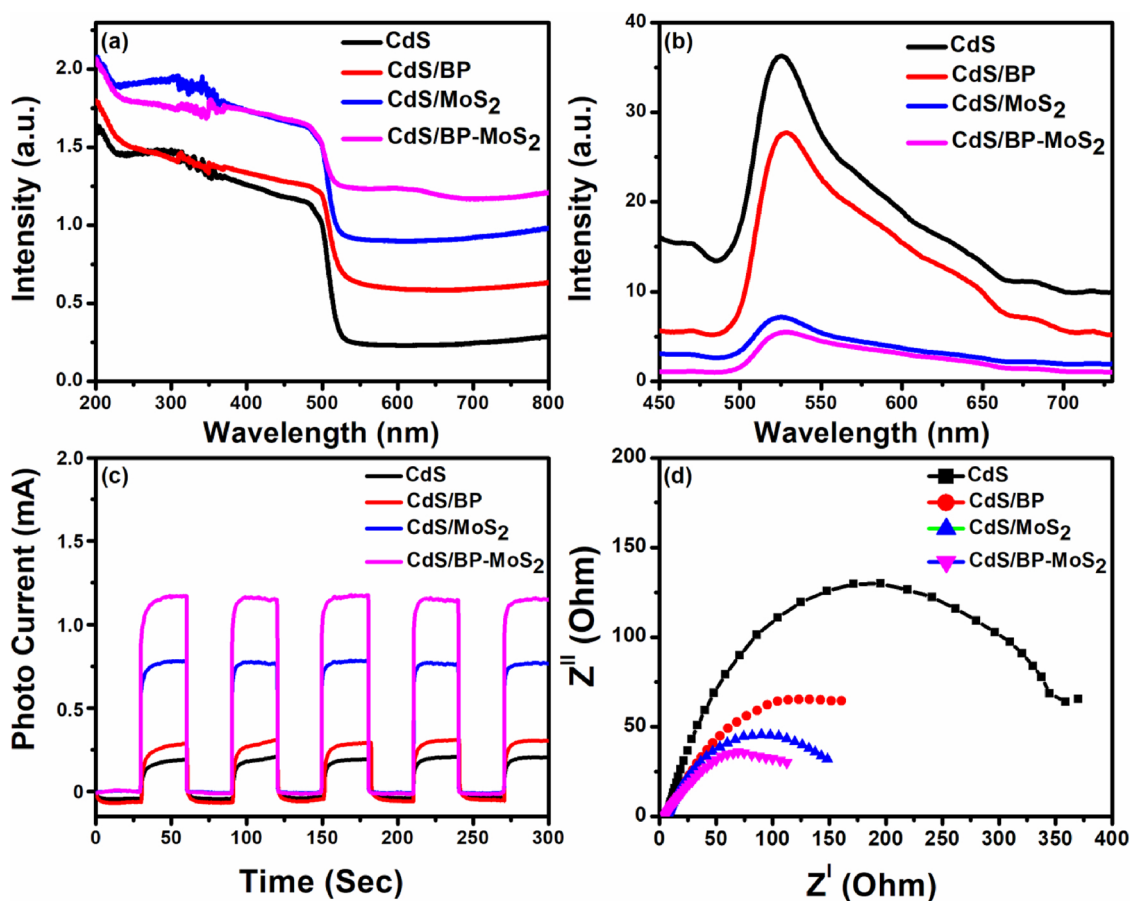

Fig. 4. (a) DRS, (b) PL, (c) photocurrent, and (d) impedance measurements of CdS, CdS/BP, CdS/MoS_2 and CdS/BP-MoS_2 nanohybrids.

carriers' separations and migrations, the CB values of all nanocomposites were measured using Mott-Schottky analysis (Figs. S18 and S19) [13,38]. CB values of BP, BP-MoS$_2$ and CdS were estimated to be -0.47 V, -0.21 V and -0.59 V versus RHE, respectively. We noticed that the CB potential of BP-MoS$_2$ is much lower than CdS, but more negative than the water reduction potential, suggesting that the excited electrons in CdS can easily transfer to the BP-MoS$_2$ (thus prolong the life-time of photo-generated electrons) and contribute to high H$_2$ production rate under sunlight irradiation. To gain the better understandings of band structures of relevant nanostructures, we constituted the schematic energy diagram (Fig. S20), based on the flat-band potentials and energy band gap values, which were determined from Mott-Schottky analysis (Fig. S19) and diffuse reflectance spectroscopy (DRS) (Fig. 4(a)) measurements, respectively. It is evident that the CB flat band potential of CdS nanorods slightly shifts to the positive direction (from -0.846 V to -0.682 V vs NHE at pH = 7) when forming the nanocomposites with BP-MoS$_2$. The positive shift may be due to efficient close interfacial contact between CdS nanorods and BP-MoS$_2$ nanostructures. When such interfacial contact was made, the photogenerated electrons from the CB of CdS can flow to the CB of BP-MoS$_2$, which can lower their energy resulting potential drop arise across the junction between CdS and BP-MoS$_2$. This potential drop may lead continuously to the equilibrium of CdS with the Fermi level of BP-MoS$_2$. Moreover, this potential drop may cause the deformation of the band structure. We expect that the deformation of band structure and positive shift may significantly contribute the efficient photocatalytic processes [38].

CdS, CdS/BP, CdS/MoS$_2$ and CdS/BP-MoS$_2$ nanohybrids were exhaustively characterized by PL, time dependent photocurrent responses and EIS measurements (Fig. 4(b)–(d)). On 380 nm photoexcitation, CdS nanorods show an intense broad PL emission band, centered at around 525 nm, which is originated from its band edge emission upon light excitation. The intense emission band indicates that recombination of photo-process excited electron and hole pairs in CdS was very strong [36,37]. However, upon the formation of nanohybrids with BP, MoS$_2$ and BP-MoS$_2$ into the CdS, appreciable emission intensity drop and a slight red shift are noticed. Among them, CdS/BP-MoS$_2$ nanostructures show very sharp intensity drop than the other nanohybrids. This red shift may be originating from the non-covalent stacking interactions between BP-MoS$_2$ and CdS and the interfacial photo-excited electron transfer from the attached CdS to the BP-MoS$_2$ nanostructures [36,37]. Meanwhile, the appreciable PL quenches of CdS/BP-MoS$_2$ suggests the photo-induced charge carriers' recombination is greatly suppressed by the efficient charge carriers' separation. The efficient charge separations be owed to the formation of nanohybrid (BP-MoS$_2$) and CdS, which can create new surface states for photo charge carrier's traps and efficient charge transfer from CdS to BP-MoS$_2$. This is also speculated from the time dependent transient photocurrent responses (Fig. 4(c)) and linear sweep voltammetry (LSV) photocurrent intensity (Fig. S21), where the CdS/BP-MoS$_2$ nanostructures exhibit an obvious enhancement of photocurrent intensity compared to the CdS, CdS/BP and CdS/MoS$_2$ nanostructures, thus indicating an improved photo-generated charge carriers' separation. Moreover, EIS analysis (Fig. 4(d)) exhibits a smaller semicircular area for the CdS/BP-MoS$_2$ nanohybrid compared to the CdS, CdS/BP and CdS/MoS$_2$ nanostructures, evidencing that CdS/BP-MoS$_2$ exhibits the fastest interfacial photo-charge transfer due to the formation of nanohybrid and sensitized with CdS. Following the photo charge carriers separation and migration, the final contribution in solar driven photocatalytic H$_2$ production includes the surface catalytic redox reactions originated by the active sites on BP-MoS$_2$ nanohybrid. To verify this aspect, we measured the nitrogen adsorption–desorption (BET) curves. The BET results demonstrate that the surface area of the CdS/BP-MoS$_2$ nanohybrid (96.84 m^2 g^{-1}) is much higher compared to the CdS nanorods (56.3 m^2 g^{-1}), this higher specific surface area may contribute to participate a greater number of catalytically active sites to boost the solar driven hydrogen evolution.

Based on above results, a plausible mechanism for extraordinary
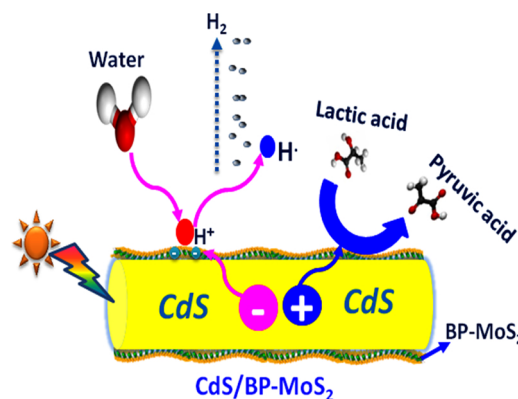
Scheme 2. Schematic illustration of photocatalytic hydrogen generation using CdS/BP-MoS$_2$ nanohybrid as a catalyst and lactic acid as a sacrificial agent under sunlight irradiation.

solar driven hydrogen evolution using CdS/BP-MoS$_2$ as a photocatalyst and lactic acid as a hole sacrificial reagent is schematically displayed in Scheme 2. Under simulated sunlight, the CdS nanohybrid absorbs the light and produce photo-generated electrons and holes in the VB and CB, respectively due to its high light harvesting capability (ranging from UV to NIR region). The available electrons from the CB of CdS are transferred to the conduction band of BP-MoS$_2$ due to their favorable band positions and high conductivity, where the protons are reduced to form molecular H$_2$ [39,40]. Meanwhile, the holes in the VB of CdS react with scavenger lactic acid, leading to the formation of intermediate products. To verify intermediates, we have measured the actual pH of the reaction solutions before and after the photocatalytic experiments and noticed the variation in pH from 2.06 to 2.13. This variation in pH indicates that the oxidized products are generated after photocatalytic reactions. Previously, Zhang et al. ascribed the pH variation before/after photocatalytic reactions to the formation of oxidized intermediates from lactic acid to pyruvic acid [41].

3. Conclusions

Herein, for the first time, a new highly robust noble-metal-free BP-MoS$_2$ nanohybrid for solar-driven hydrogen evolution by water splitting were designed and characterized. Benefiting from the rich active sites, abundant structural and compositional features, the resulting nanohybrid manifest remarkable catalytic and co-catalytic performance with high amount of H$_2$ production (CdS/BP-MoS$_2$: 186.32 mmol h^{-1} g^{-1}) and outstanding stability under simulated solar light irradiation which is 72 times higher than the CdS nanostructures. The enhanced H$_2$ production rate is due to their highly active catalytic sites, high light harvesting capacity and efficient charge recombination rate which are experimentally verified and discussed in detail. In addition, the role of catalyst dosage and hole scavenger concentration for the photocatalytic efficiency are thoroughly verified. Finally, we expect that the demonstrated new heterostructured design strategy may bring novel insights to develop low-price noble metal free photocatalysts for solar driven hydrogen evolution.

Appendix A. Supplementary data

Supplementary material related to this article can be found, in the online version, at doi:https://doi.org/10.1016/j.apcatb.2018.09.055.

References

[1] K.C. Christoforidis, P. Fornasiero, ChemCatChem 9 (2017) 1523–1544.
[2] X. Chen, S. Shen, L. Guo, S.S. Mao, Chem. Rev. 110 (2010) 6503–6570.
[3] A. Naseri, M. Samadi, A. Pourjavadi, A.Z. Moshfegh, S. Ramakrishna, J. Mater. Chem. A Mater. Energy Sustain. 5 (2017) 23406–23433.
[4] Z. Hu, Z. Shen, J.C. Yu, Green Chem. 19 (2017) 588–613.
[5] Y. Xu, Y. Huanga, B. Zhang, Inorg. Chem. Front. 3 (2016) 591–615.
[6] N. Singh, J. Prakash, R.K. Gupta, Mol. Syst. Des. Eng. 2 (2017) 422–439.
[7] M.D. Hernandez-Alonso, F. Fresno, S. Suarez, J.M. Coronado, Energy Environ. Sci. 2 (2009) 1231–1257.
[8] K. Maeda, Kazunari Domen, J. Phys. Chem. Lett. 1 (2010) 2655–2661.
[9] K. Takanabe, ACS Catal. 7 (2017) 8006–8022.
[10] S.K. Muduli, E. Varrla, Y. Xu, S.A. Kulkarni, A. Katre, S. Chakraborty, S. Chen, T.C. Sum, R. Xu, N. Mathews, J. Mater. Chem. A Mater. Energy Sustain. 5 (2017) 24874–24879.
[11] J. Kim, S.S. Baik, S.H. Ryu, Y. Sohn, S. Park, B.-G. Park, J. Denlinger, Y. Yi, H.J. Choi, K.S. Kim, Science 349 (2015) 723–726.
[12] M.Z. Rahman, C.W. Kwong, K. Davey, S.Z. Qiao, Energy Environ. Sci. 9 (2016) 709–728.
[13] X. Zhu, T. Zhang, Z. Sun, H. Chen, J. Guan, X. Chen, H. Ji, P. Du, S. Yang, Adv. Mater. 29 (2017) 1605776.
[14] X. Zhang, Z. Zhang, S. Zhang, D. Li, W. Ma, C.X. Ma, F. Wu, Q. Zhao, Q. Yan, B. Xing, Small 13 (2017) 1701210.
[15] M. Zhu, S. Kim, L. Mao, M. Fujitsuka, J. Zhang, X. Wang, T. Majima, J. Am. Chem. Soc. 139 (2017) 13234–13242.
[16] M. Zhu, C. Zhai, M. Fujitsuka, T. Majima, Appl. Catal. B 221 (2018) 645–651.
[17] J. Ran, X. Wang, B. Zhu, S.Z. Qiao, Chem. Commun. 53 (2017) 9882–9885.
[18] M. Zhu, Y. Osakada, S. Kim, M. Fujitsuka, T. Majima, Appl. Catal. B 217 (2017) 285–292.
[19] J. Ran, B. Zhu, S.Z. Qiao, Angew. Chem. Int. Ed. 56 (2017) 10373–10377.
[20] M. Zhu, X. Cai, M. Fujitsuka, J. Zhang, T. Majima, Angew. Chem. Int. Ed. 56 (2017) 2064–2068.
[21] R. He, J. Hu, A. Zhang, C. Wang, J. Peng, W. Chen, J. Zeng, Nano Lett. 17 (2017) 4311–4316.
[22] Y. Deng, Z. Luo, N.J. Conrad, H. Liu, Y. Gong, S. Najmaei, P.M. Ajayan, J. Lou, X. Xu, P.D. Ye, ACS Nano 8 (2014) 8292–8299.
[23] J. Xu, J. Jia, S. Lai, J. Ju, S. Lee, Appl. Phys. Lett. 110 (2017) 033103.
[24] T. Hong, B. Chamlagain, T. Wang, H.J. Chuang, Z. Zhou, Y.Q. Xu, Nanoscale 7 (2015) 18537–18541.
[25] P. Chen, J. Xiang, H. Yu, J. Zhang, G. Xie, S. Wu, X. Lu, G. Wang, J. Zhao, F. Wen, Z. Liu, R. Yang, D. Shi, G. Zhang, 2D Mater. 2 (2015) 034009.
[26] S.H. Aldave, M.N. Yogeesh, W. Zhu, J. Kim, S.S. Sonde, A.P. Nayak, D. Akinwande, 2D Mater. 3 (2016) 014007.
[27] D.A. Reddy, H.K. Kim, Y. Kim, S. Lee, J. Choi, M.J. Islam, D.P. Kumar, T.K. Kim, J. Mater. Chem. A Mater. Energy Sustain. 4 (2016) 13890–13898.
[28] D.A. Reddy, J. Choi, S. Lee, Y. Kim, S. Hong, D.P. Kumar, T.K. Kim, Catal. Sci. Technol. 6 (2016) 6197–6206.
[29] D.A. Reddy, H. Park, M. Gopannagari, E.H. Kim, S. Lee, D.P. Kumar, T.K. Kim, ChemSusChem 11 (2018) 245–253.
[30] X. Zong, H. Yan, G. Wu, G. Ma, F. Wen, L. Wang, C. Li, J. Am. Chem. Soc. 130 (2008) 7176–7177.
[31] P. Qiu, C. Xu, N. Zhou, H. Chen, F. Jiang, Appl. Catal. B 221 (2018) 27–35.
[32] J. Choi, D.A. Reddy, N.S. Han, S. Jeong, S. Hong, D.P. Kumar, J.K. Song, T.K. Kim, Catal. Sci. Technol. 7 (2017) 641–649.
[33] D.P. Kumar, H. Park, E.H. Kim, S. Hong, M. Gopannagari, D.A. Reddy, T.K. Kim, Appl. Catal. B 224 (2018) 230–238.
[34] P. Ravi, V.N. Rao, M.V. Shankar, M. Sathish, Int. J. Hydrogen Energy b43 (2018) 3976–3987.
[35] X. Zhang, Z. Zhang, S. Zhang, D. Li, W. Ma, C.X. Ma, F. Wu, Q. Zhao, Q. Yan, B. Xing, Small 13 (2017) 1701210.
[36] D.A. Reddy, H. Park, R. Ma, D.P. Kumar, M. Lim, T.K. Kim, ChemSusChem 10 (2017) 1563–1570.
[37] D.A. Reddy, H. Park, S. Hong, D.P. Kumar, T.K. Kim, J. Mater. Chem. A Mater. Energy Sustain. 5 (2017) 6981–6991.
[38] I. Vamvasakis, B. Liu, G.S. Armatas, Adv. Funct. Mater. 26 (2016) 8062–8071.
[39] W. Shangguan, J. Phys. Chem. B 106 (2002) 12227–12230.
[40] M.R. Gholipour, C.T. Dinh, F. Beland, T. Do, Nanoscale 7 (2015) 8187–8208.
[41] W. Zhang, Y. Wang, Z. Wang, Z. Zhong, R. Xu, Chem. Commun. (Camb.) 46 (2010) 7631–7633.